ACS OMEGA

http://pubs.acs.org/journal/acsodf

Article

$FeCO_3$ Synthesis Pathways: The Influence of Temperature, Duration, and Pressure

Randi Neerup, Isaac A. Løge, and Philip L. Fosbøl*

Cite This: *ACS Omega* 2023, 8, 3404−3414

Read Online

ACCESS | Metrics & More | Article Recommendations

ABSTRACT: $FeCO_3$ is present as scales in process equipment, corrosion products, geological systems, and carbon storage. It is therefore crucial to investigate the properties of $FeCO_3$ to understand scaling in all these systems. However, $FeCO_3$ is not commercially available, and when used in the lab it is either obtained through extraction of geological formations or synthesized in-house. Geologically formed $FeCO_3$ contains multiple impurities, which will affect its overall properties, and the synthesized product is highly sensitive to either oxidation or the synthesis pathways. This work explores the parameter space of a synthesis route routinely and pathways for $FeCO_3$. We characterized the structure of $FeCO_3$ using X-ray powder diffraction and its thermal properties with thermogravimetric analysis and scanning electron microscopy. We show how synthesis parameters influence either the macroscopic or microscopic properties of the synthesized product. Our study serves as a guideline for future research regarding what parameters to choose when synthesizing $FeCO_3$ and what product can be obtained. We herein present a novel fundamental understanding of $FeCO_3$.

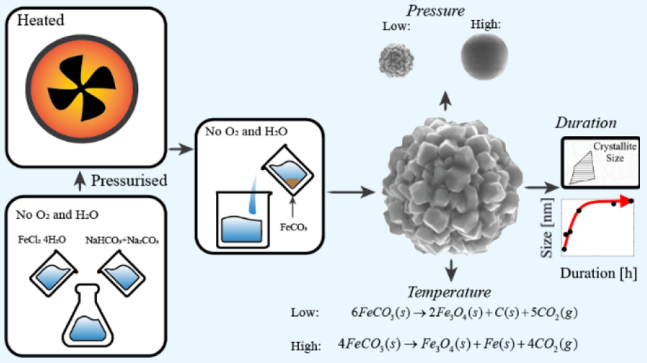

1. INTRODUCTION

$FeCO_3$ has attracted considerable attention as this mineral is related to CO_2 capture, the carbon cycle of the earth, natural protection against corrosion, and much more.[1−18]

However, in each scenario, a different physicochemical property of $FeCO_3$ is involved. The following section will be an introduction to various areas in which $FeCO_3$ is present, followed by the existing knowledge on $FeCO_3$ synthesis. Discrepancies are discussed along with their possible explanations.

Through the carbon cycle of the earth, tectonic plates are known to subduct carbon into the upper and lower mantle. Here, carbon can be stored in the form of divalent metal carbonate composites such as $MgCO_3$, $FeCO_3$, and $CaCO_3$.[2] At high-pressure conditions of the lower mantle, iron has been reported to make a spin transition; however, variations in the pressure at which this transition occurs have been reported.[12] This transition is associated with changes in physical properties such as conductivity, sound velocity, and volume. There have been controversies regarding the exact pressure under which this transition takes place. Stekiel et al.[15] showed that these discrepancies could be a result of mixing Mg into the $FeCO_3$ lattice. The real basis for the investigation of these phenomena can only be determined if $FeCO_3$ formation can be controlled correctly.

Human-engineered underground carbon storage has been proposed as a possible tool to mitigate anthropogenic greenhouse gas emissions. Mineralization of basaltic glass, basaltic rocks, serpentine rocks, and peridotite rocks[19] through injection of CO_2 is one of the possible solutions. Injection of CO_2 directly into the underground would be an acceleration of the natural processes and could be a permanent and safe storage activity.[20,21] In the CarbFix pilot project, CO_2 is captured from a geothermal power plant in Iceland and injected in situ into basaltic rocks.[20,21] To understand this mineralization, the formation kinetics of $FeCO_3$ must be understood. Recently, the role of $FeCO_3$, as a reversible sorbent, has been investigated. However, due to kinetic limitations during the synthesis of $FeCO_3$, the optimal CO_2 storage capacity could not be obtained.[11,22]

Corrosion is one of the major limitations during capture and transport of CO_2. This is a general phenomenon, observed in anoxic conditions in production equipment. When CO_2 interacts with water, it results in the formation of carbonic acid. This is highly corrosive toward metals, resulting in vast economic loss, as the equipment lifetime gets shortened.

Received: November 14, 2022
Accepted: December 15, 2022
Published: January 10, 2023

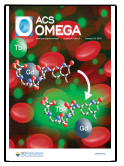

Table 1. Literature Review on $FeCO_3$ Synthesis. NA = Not Available

reference	reactants	reaction parameters			color
		T (°C)	P (bar)	time (h/days)	
Smith[30]	$FeSO_4$ and $NaHCO_3$ mixed with water saturated with CO_2	100	27.6	several days	white
Sharp[31]	$FeSO_4{\cdot}7H_2O$ and $NaHCO_3$ mixed in water; CO_2 (g) pumped into the sealed bomb	200	500	3 days	oxidized to yellow-brown
Graf[37]	(1) $FeSO_4$, Na_2CO_3, CO_2, and water	(1) 300	(1 + 2) 14,000	(1) 15 h	NA
	(2) $FeSO_4$, Na_2CO_3, $NaHCO_3$, CO_2, and water	(2) 659		(2) 3 h	
Johannes[58]	$CaCO_3$ + $FeCl_2$	150−300	1000		NA
Gould[59]	Fe wire and CO_2	25	NA	>24 h	NA
Singer and Stumm[27]	excess of $FeClO_4$ and $NaHCO_3$ added to an $HClO_4$ solution; system flushed with N_2 to remove oxygen.	NA	NA	1−5 month	NA
Chai and Navrotsky[55]	Fe(II) oxalate and CO_2 (g)	360	1000−2000	48 h	tan
Gramsjäger and Reiterer[60]	$FeCl_2$ mixed with HCl, urea, and solid CO_2 in an autoclave	140−160	40−80	30−50 h	NA
Ehrhardt et al.[56]	$FeC_2O_4{\cdot}2H_2O$ mixed with CO_2 (g)	415 and 470	3800 and 3500	24 h	beige
Ehrhardt et al.[38]	(1) $FeSO_4{\cdot}7H_2O$ mixed with CO_2	(1) 180	(1) 1200	(1) 48 h	colorless
	(2) $Fe(OH)_2$ mixed with CO_2	(2) 150	(2) 2500	(2) 30 h	
Wajon et al.[50]	bubbling CO_2 through a suspension of iron filings	NA	NA	NA	green
Greenberg and Tomson[39]	Mohr's salt, CO_2, and $NaHCO_3$ mixed with deoxygenated deionized water.	ambient temperature	NA	NA	light to gray
Stubina and Toguri[61]	reacting $FeCl_2{\cdot}4H_2O$ crystals with $CaCO_3$ powder	170	NA	24 h	NA
Lyon[62]	$FeCl_2{\cdot}4H_2O$ + $NaHCO_3$ in different molar ratios mixed with degassed water	200	NA	16−70 h	bluish gray, white, beige
Wersin et al.,[40] Bruno et al.[41]	CO_2-saturated $FeSO_4$−$NaHCO_3$ solution	100	19	24 h	beige
Johnson,[57] Tomson and Johnson[52]	$NaHCO_3$ and Mohr's mixed with deoxygenated deionized water.	NA	NA	2 h	white
Ptacek[53]	mixing $FeCl_2{\cdot}4H_2O$ and $Na_2CO_3/NaHCO_3$ in a glovebox in a 1:4 molar ratio; addition of HCl.	160	NA	several days	white
Heuer and Stubbins[42]	mixture of 0.5 M ferrous ammonium sulfate and 0.75 M sodium bicarbonate	75	NA	48 h	white
Silva et al.[63]	Ferrous sulfate heptahydrate and sodium bicarbonate mixed with deoxygenated Milli-Q water according to the method of Greenberg and Tomson[39]	NA	NA	NA	NA
Jimenez-Lopez and Romanek,[64] Romanek et al.[65]	$NaHCO_3$ and $Fe(ClO_4)_2$ mixed with degassed distilled water in an anaerobic chamber.	25	1	NA	NA
Gogolev et al.[33]	Mohr's salt added to 1−3 M $KHCO_3$ in the absence of oxygen	NA	NA	NA	white
Chirita et al.,[43,44] Kiss et al.,[32] Gogolev et al.[33]	ferric ammonium sulfate, Na_4EDTA, and urea mixed with deionized water; pH adjusted to 6 with HCl.	250	NA	22 h	NA
Zhong et al.[46]	$FeCl_3{\cdot}6H_2O$, urea, and ascorbic acid dissolved and mixed with deionized water.	160	NA	3 h	NA
Liu et al.[45]	$FeCl_3{\cdot}6H_2O$, urea, ascorbic acid, and polyvinylpyrrolidone dissolved and mixed in deionized water.	160	NA	6 h	black
Sánchez-Alcalá et al.[35]	pilot experiment; $FeSO_4{\cdot}7H_2O$ and K_2CO_3 mixed with water.	NA	NA	NA	pale brown/green
Yang et al.[34]	$FeSO_4{\cdot}7H_2O$, ascorbic acid, and urea mixed with deionized water.	160	NA	3 h	NA
Zhang et al.[9]	sodium dodecyl sulfate, $FeSO_4{\cdot}7H_2O$, and urea mixed with deionized water; pH adjusted to 4 with HCl.	100	NA	4 h	NA
Kang et al.[54]	iron oxalate dehydrate sealed in a gold capsule.	350	2000	120 h	gray-white to slightly brownish
Figueiredo et al.[47]	$FeCl_2{\cdot}4H_2O$ and $NaHCO_3$ mixed with deoxygenated water.	50	NA	12 h	light green
Feng et al.[48]	urea, $FeCl_3$, and ascorbic acid dissolved and mixed in distilled water.	160	NA	6 h	NA
Liu et al.[10]	$Fe(NO_3)_3{\cdot}9H_2O$, $CO(NH_2)_2$ or NH_4HCO_3, ethylene glycol, and ascorbic acid dissolved and mixed in water.	160	NA	5 h	NA
Liang et al.[49]	$FeC_2O_4{\cdot}2H_2O$ sealed into a silver capsule and using NaCl as the pressure transmitting medium; graphite is used as a furnace; high-pressure synthesis performed on a cubic anvil apparatus.	NA	NA	1 h	NA
Koo and Kim[66]	$FeCl_2{\cdot}4H_2O$ and $NaHCO_3$ mixed with degassed distilled water in an anaerobic chamber.	30	NA	1 week, 1 month	NA

$FeCO_3$ is obtained as a byproduct of corrosion and can create a protective barrier against further corrosion. However, the protective properties depend on the solution and surface conditions. The exact kinetics of $FeCO_3$ formation have been investigated but not completely understood.[23,24]

$FeCO_3$ is also present as an iron source for industry producing animal feed,[25] as a soil stabilizer in agriculture,[26] as a redox active component in groundwater,[27−29] and as a potential anode material in lithium-ion batteries.[9,10]

1.1. Existing Knowledge of $FeCO_3$ Synthesis. The synthesis of $FeCO_3$ is a key aspect for understanding the

https://doi.org/10.1021/acsomega.2c07303
ACS Omega 2023, 8, 3404−3414

mechanisms behind corrosion and mineralization, as well as using $FeCO_3$ in agriculture and the feed industry. $FeCO_3$ cannot be bought commercially; it needs to be produced in-house or extracted from rock materials. The main challenge of synthesizing $FeCO_3$ is that it reacts rapidly with oxygen at low concentrations.

Methods of synthesizing $FeCO_3$ are well documented. In the review by Fosbøl et al.,[5] methods of synthesizing $FeCO_3$ until 2006 are summarized and discussed. Table 1 gives an overview of available literature data on $FeCO_3$ synthesis pathways based on the review by Fosbøl et al.[5] The table has extensive data from literature from 2007 until today. Reactants, reaction time, synthesis temperature, and pressure are listed in the table.

The synthesis routes vary concerning the iron and carbonate sources. In most of the literature, the iron source is a salt of SO_4, Cl_2, ClO_4, NO_3, and C_2O_4, whereas the carbonate source is urea, CO_2 (g), bicarbonate, carbonate, and oxalate. As indicated in Table 1, there is a large variation in synthesis method parameters. In general, the synthesis methods can be divided into four categories:

1. Ambient conditions and short reaction time (approximately 24 h)
2. High pressure, high temperature, and long reaction time
3. High pressure, high temperature, and short reaction time
4. High temperature and short reaction time (3−12 h)

The outcome of the variation in the synthesis temperature, pressure, reaction time as well as iron and carbonate sources is variation in quality. The produced $FeCO_3$ differs in morphology, and the color changes from white/beige to black, green, and blue. In most of the literature,[30−44] $FeSO_4$ or Mohr's salt is used as an iron source for producing $FeCO_3$ (see Table 1).

Some authors[10,34,36,37,45−49] have used high temperatures and long reaction times in the range of 1−12 h. In some cases, short reaction times seem to result in $FeCO_3$ of a slightly greenish color, from chloride, which indicates that the reaction is not complete.[47,50,51]

In many of the cases, the product has been influenced by oxygen, which can be observed as orange to black crystals.[31,45] Most often, $FeCO_3$ is obtained as white to beige crystals.[30,33,35,39−42,52−57] In general, there is an absence of detailed information describing the color of the synthesized product. Visual inspection of the product gives a clear indication of whether the synthesis has been performed under the absorption of oxygen. In some cases, the reaction temperature and time are not mentioned in the literature. The method mentioned in these studies cannot be used for producing $FeCO_3$.

This work aims to characterize the physicochemical properties of synthesized $FeCO_3$ by exploring the parameter space spanning the temperature, pressure, and synthesis duration.[67] We present a visual inspection, where the color and agglomeration of the synthesized product are commented on. We used scanning electron microscopy (SEM), X-ray powder diffraction (XRPD), and thermogravimetric analysis (TGA) to investigate the microscopic and macroscopic sizes, which are linked to the thermal properties of the obtained product. This will, in turn, provide basic knowledge of a more consistent method for synthesizing $FeCO_3$.

2. MATERIALS AND METHODS

2.1. Materials. $FeCl_2{\cdot}4H_2O$, $NaHCO_3$, and Na_2HCO_3 were obtained from Sigma-Aldrich and used without further purification, see Table 2. Stock solutions from $FeCl_2{\cdot}4H_2O$, $NaHCO_3$, and Na_2HCO_3 were prepared with ultra-pure Milli-Q water, and before mixing they were degassed with N_2 (>99.999%, AGA) for approximately 1 h until an oxygen level less than 0.07 mg/L was obtained. The concentration of dissolved oxygen (DO) was measured with a multi-meter (Hach Lange, HQ40D) connected to a DO sensor (Hach Lange, LDO101).

Table 2. Chemicals Used for $FeCO_3$ Synthesis

chemical name	source	CAS no.	mass fraction purity (%)	purification method
iron(II) chloride tetrahydrate	Sigma-Aldrich	13478-10-9	≥99.0	none
sodium bicarbonate	Sigma-Aldrich	144-55-8	≥99.0	none
sodium carbonate	Sigma-Aldrich	497-19-8	≥99.0	none

2.2. $FeCO_3$ Synthesis. The synthesis of $FeCO_3$ was based on the study by Murcia.[51] $FeCO_3$ synthesis was performed in a glovebox (MBRaun), which was filled with a H_2/N_2 (H_2, 10.0100422%) atmosphere. The atmosphere inside the glovebox was continuously circulated via a catalyst to trap oxygen and water. The concentration levels of oxygen and H_2O were monitored by O_2 and H_2O gas analyzers (MBRaun).

Aqueous solutions of $FeCl_2{\cdot}4H_2O$ and $NaHCO_3/Na_2CO_3$ were prepared with a Fe/CO_2 mole ratio of 1:4 on a balance with an accuracy of 0.1 mg. Both solutions were loaded into a titanium piston cylinder, which beforehand was evacuated using a vacuum pump. The cylinder was taken out of the glovebox, pressurized, and then placed in an oven at a constant temperature. The reaction was terminated by taking the cylinder out of the oven and letting it cool to room temperature by blowing air over the cylinder. The cooling took approximately 1 h. The cooled cylinder was transported back to the glovebox, where the supernatant was decanted and the $FeCO_3$ was carefully washed with deoxygenated Milli-Q water. $FeCO_3$ was allowed to dry in the glovebox for 2 to 3 days.

The adjustable synthesis parameters which are temperature, pressure, and reaction time are summarized in Table 3.

The overall carbon content in the initial phase of the synthesis is well determined from the procedure. The CO_2 concentration will vary throughout the reaction depending on the extent of the reaction. In the presented procedure, the pressure was maintained during synthesis. For this reason, we expect the free CO_2 (aq) content in the liquid phase to be constant. We estimate this to be in the order of 0.01 to 1 wt % based on the temperature and pressure applied.

2.3. Sample Characterization Methods. Synthesized $FeCO_3$ was verified and characterized using XRPD, SEM, and TGA. The characterization methods are hereafter described.

2.3.1. X-ray Powder Diffraction. The crystal structure of $FeCO_3$ was determined by XRPD at room temperature. The powder diffraction patterns were collected with a Huber G670 powder diffractometer in the 2θ range of 3 to 100° in steps of

https://doi.org/10.1021/acsomega.2c07303
ACS Omega 2023, 8, 3404−3414

Table 3. Parameters for $FeCO_3$ Synthesis

Fe/CO_2 ratio	temperature (°C)	pressure (bar)	reaction time (h)
1:4	25	10	24
1:4	80	10	24
1:4	130	10	24
1:4	130	1	24
1:4	130	5	24
1:4	130	15	24
1:4	130	10	4
1:4	130	10	6
1:4	130	10	12
1:4	130	10	24
1:4	130	10	72
1:4	130	10	96

0.005° using Cu Kα1 radiation (λ = 1.54056 Å) for 10 min. The data were collected in the transmission mode from a rotating flat plate sample inclined 45° relative to the primary beam.

Crystalline sizes were determined from the diffractograms via the Scherrer equation. To obtain the sizes through the Scherrer equation, the diffractograms were fitted to Gaussian first-order models from which the full width at half-maximum (fwhm) was determined. The Scherrer equation is defined as

$$\tau = \frac{K\lambda}{\beta\theta} \quad (1)$$

where τ is the mean size of ordered (crystalline) domains, K is a dimensionless shape factor, λ is the X-ray wavelength, β is the line broadening at half the maximum intensity (fwhm), and θ is the Bragg angle.

2.3.2. Scanning Electron Microscopy. SEM images were acquired in an FEI QEISCAN with an acceleration voltage of 20 kV under a high vacuum. Samples were transported in an airtight environment from the glovebox to the scanning electron microscope. During transfer to the scanning electron microscope environment, the samples were exposed to atmospheric conditions for less than 1 min.

The images were analyzed in ImageJ and Gwyddion to obtain the particle sizes. Size distributions were obtained by measuring the diameter of more than 400 particles on each set of data.

2.3.3. Thermogravimetric Analysis. The decomposition of $FeCO_3$ was performed using TGA (TA Instruments, Discovery TGA). Measurements were conducted in a nitrogen atmosphere in a temperature range of 27−900 °C with a temperature ramp rate of 10 °C/min.

3. RESULTS AND DISCUSSION

3.1. Visual Inspection of Color and Agglomeration. Optimal operating conditions for obtaining high-purity $FeCO_3$ are of great importance, as the quality of the product depends not only on the iron and CO_2 sources but also on synthesis parameters such as the temperature, reaction time, and pressure.

$FeCO_3$ was synthesized by varying the reaction time (Figure 1), pressure (Figure 2), and temperature (Figure 3). The color of the precipitating $FeCO_3$ was found to have nuances of beige. By visually inspecting the color of the product, there is a clear tendency that by increasing the reaction time and the temperature, the color changes from light to darker beige. At 25 °C, the produced $FeCO_3$ had a green/beige color indicating that not all the $FeCl_2{\cdot}4H_2O$ had reacted with the $NaHCO_3$/Na_2CO_3 solution (see Figure 3). The color seemed to go from dark to light beige, increasing the pressure of the $FeCO_3$ synthesis. $FeCO_3$ synthesized at a pressure of 5 bar (from nitrogen) is deviating from the observed. At 5 bar, the product color is much brighter than expected, compared to $FeCO_3$ synthesized at 1, 10, and 15 bar. The reason for the color deviation might be a result of the method on mixing the used chemicals. If the used reagents were different from one batch to the next, it could impact the final precipitated product.

The $FeCO_3$ grains produced at a synthesis duration of 4−6 h at 1−5 bar and 25 °C (Figures 1−3) seemed to be flakier in nature. High pressure or longer reaction time seems to give a fine powder-like product. The slurry was not stirred or mechanically grinded, and the drying was performed on a stagnant plate without vacuum filtration. The reason for the significant difference in product characteristics could be a result of the CO_2 impacting the crystallization process. The fine particles were re-crystallized during the longer reaction time or as a consequence of higher CO_2 pressure. A higher synthesis temperature also gave a fine powder-like product (Figure 3), as the reaction kinetics are faster at higher temperatures.

3.2. Electron Microscopy Observations. $FeCO_3$ is reported to take a rhombohedral shape associated with that of carbonate crystals. In this study, we observed a hierarchical growth where larger spherical particles were present with rhombohedral crystals growing on their surface, as presented in Figure 4A−D, similar to Kim et al.[71] We observe the particle to be spherical, where there is a tendency for the spheres to merge. Figure 4A shows a magnification of the rhombohedral crystals, which have nucleated on the surface of the spherical particle. It was assumed that the particles act as a nucleation

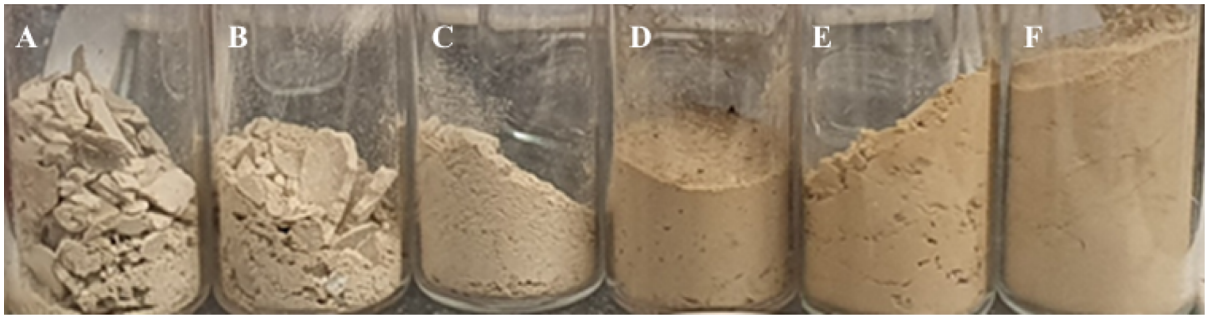

Figure 1. $FeCO_3$ product synthesized at 10 bar and 130 °C. The synthesis has been carried out as a function of reaction time. (A) 4, (B) 6, (C) 12, (D) 24, (E) 72, and (F) 96 h.

https://doi.org/10.1021/acsomega.2c07303
ACS Omega 2023, 8, 3404−3414

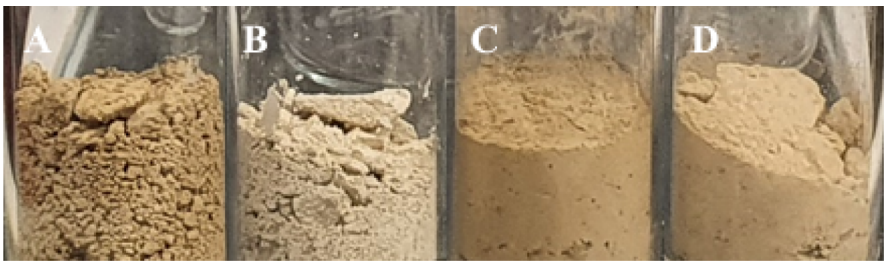

Figure 2. $FeCO_3$ product synthesized at 24 h and 130 °C. The synthesis has been carried out as a function of pressure. (A) 1, (B) 5, C) 10 bar (different batch compared to Figure 1), and (D) 15 bar.

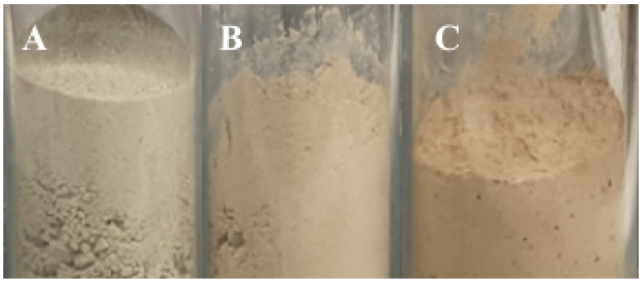

Figure 3. $FeCO_3$ product synthesized at 10 bar and 24 h. The synthesis has been carried out as a function of temperature. (A) 25, (B) 80, and (C) 130 °C (different batch, compared to Figures 1 and 2).

site for smaller $FeCO_3$ crystals. These spherical particles were previously reported in the literature[68] to be amorphous $FeCO_3$ (AFC). In the present work, the particles were analyzed by means of transmission electron microscopy (TEM). The TEM analysis showed that these particles do in fact exhibit crystallinity and therefore cannot be AFC (see Figure 4B). As these particles are too large to be individual single crystals, in this study, the following terminology will be used throughout. From Figure 4D, the diameter of the large particle has been referred to as the particle size, while the individual crystallites which can also be seen on the surface are called either by the crystallite size or by the scattering coherence length. It has not been possible to characterize a trend of crystallite sizes or surface morphology from the SEM images. Instead, the crystallite and particle sizes are determined as a function of synthesis parameters, as presented in the following sections.

Increasing temperature, pressure, and synthesis reaction time seem to be important factors in controlling the nanostructure of $FeCO_3$. Three nanostructures were identified. Among these morphologies, rhombohedral-shaped structures were seen, which is in accordance with literature.[68,69] These crystals are shown in Figure 4C,D. Additionally, flower-like structures (Figure 4D) and almost perfectly shaped circular globes (Figure 4C) were identified.

3.3. Impact of Temperature during $FeCO_3$ Crystallization. *3.3.1. Microscopic Properties.* The composition of the synthesized $FeCO_3$ was identified with XRPD, and the spectra at 25, 80, and 130 °C are presented in Figure 5b. For

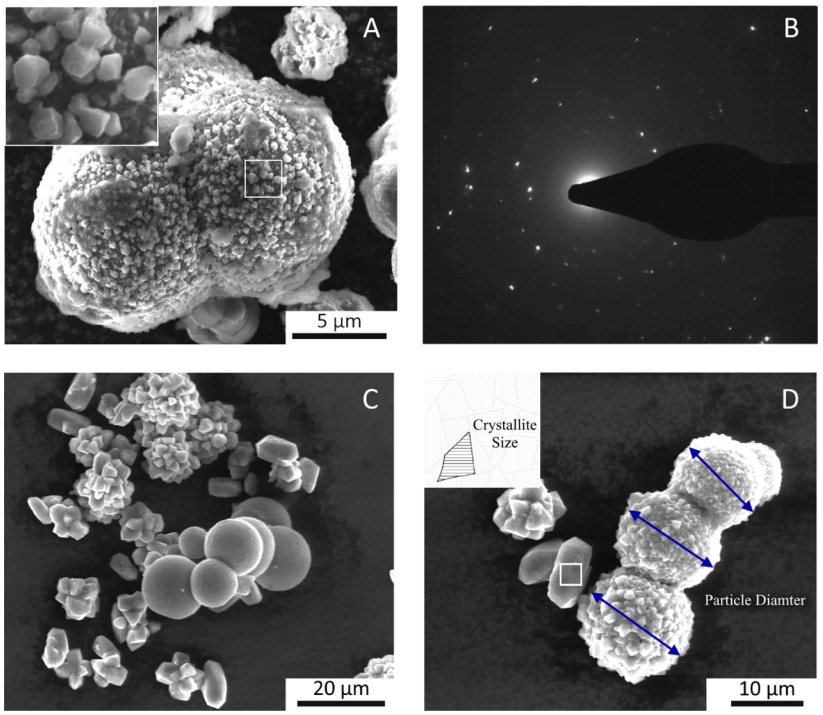

Figure 4. SEM image of $FeCO_3$ visualizing various grain morphologies. (A) Hierarchical structure, with the inset showing cubing structures on the surface of a larger grain, (B) selective area diffraction patterns of $FeCO_3$ particles, (C) circular globe structure, and (D) flower-like structure.

https://doi.org/10.1021/acsomega.2c07303
ACS Omega 2023, 8, 3404−3414

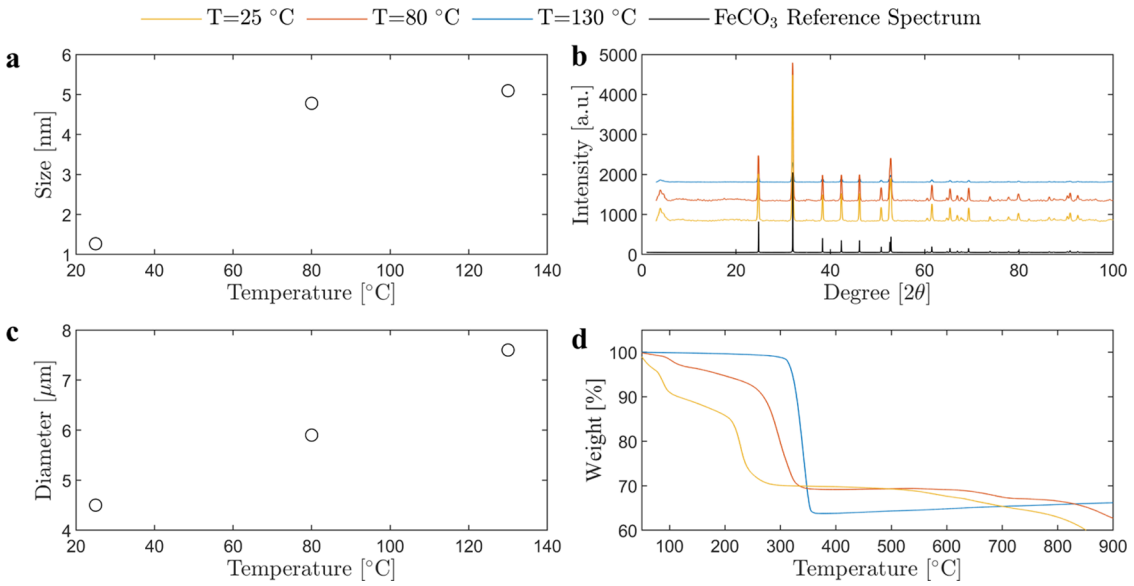

Figure 5. (a) Particle size (nm) as a function of temperature, (b) XRPD spectra of $FeCO_3$ synthesized at 10 bar for 24 h and at 25, 80, and 130 °C, (c) particle diameter (μm) as a function of temperature, and (d) TGA curves of $FeCO_3$.

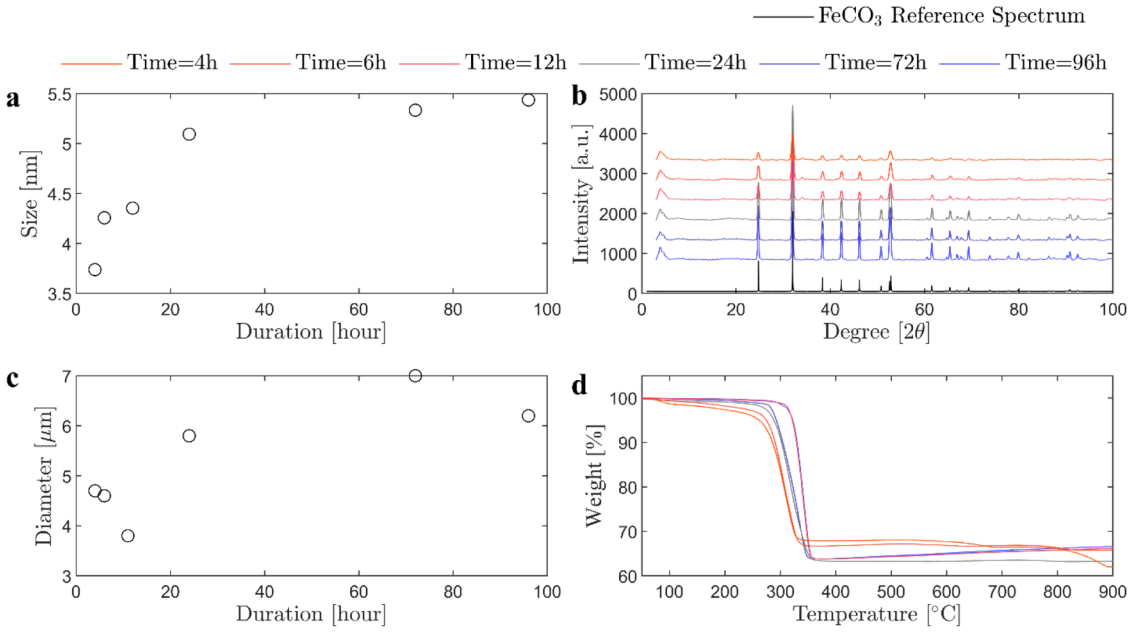

Figure 6. (a) Particle size (nm) as a function of synthesis duration, (b) XRPD spectra of $FeCO_3$ synthesized at 10 bar and 130 °C as a function of synthesis reaction time, (c) particle diameter (μm) as a function of synthesis duration, and (d) TGA curves of $FeCO_3$.

the product synthesized at 25 °C (yellow spectrum) and 80 °C (red spectrum), two additional peaks compared to the reference spectra for $FeCO_3$ were identified at 2θ = 29° and at 2θ = 34°. These can be attributed to unreacted $FeCl_2$ (29°) and Na_2CO_3 (34°). The synthesis was performed at 25 °C, and the diffraction peaks were found to be broad. At 120 °C, the peak width decreased, indicating that larger crystal domains were formed (see Figure 5b). The collected spectrum at 120 °C could be indexed to $FeCO_3$ in agreement with the inorganic crystal structure database to the reference spectra (black spectra in Figure 5b). Therefore, we infer that, for the duration and temperatures investigated, the temperature has a large influence on the chemical composition of the final product. Chemical reaction rates are highly dependent on temperature,[38,55,56,62] and we show that for the reactants to fully convert to $FeCO_3$, it is therefore necessary to have a synthesis duration of 24 h and a temperature of 120 °C.

3.3.2. Particle Properties. Figure 5a,c presents the particle size and the particle diameter as a function of temperature. The crystallite size is the size of individual crystal grains calculated from the XRPD peak broadening, while the particle diameter was estimated from analysis of the SEM images. The diameter of the particles was found to increase with temperature. Generally, a larger temperature increases the nucleation rate, and thereby smaller particles are formed.[70−76] However, as shown by the XRPD, the final product was not formed, and therefore we observe the particles to increase with increasing temperature. At 120 °C, the particles have a size of 8 μm. The particles were synthesized for 24 h and are 2 μm smaller than what was reported by previous SEM investigation on particle

https://doi.org/10.1021/acsomega.2c07303
ACS Omega 2023, 8, 3404−3414

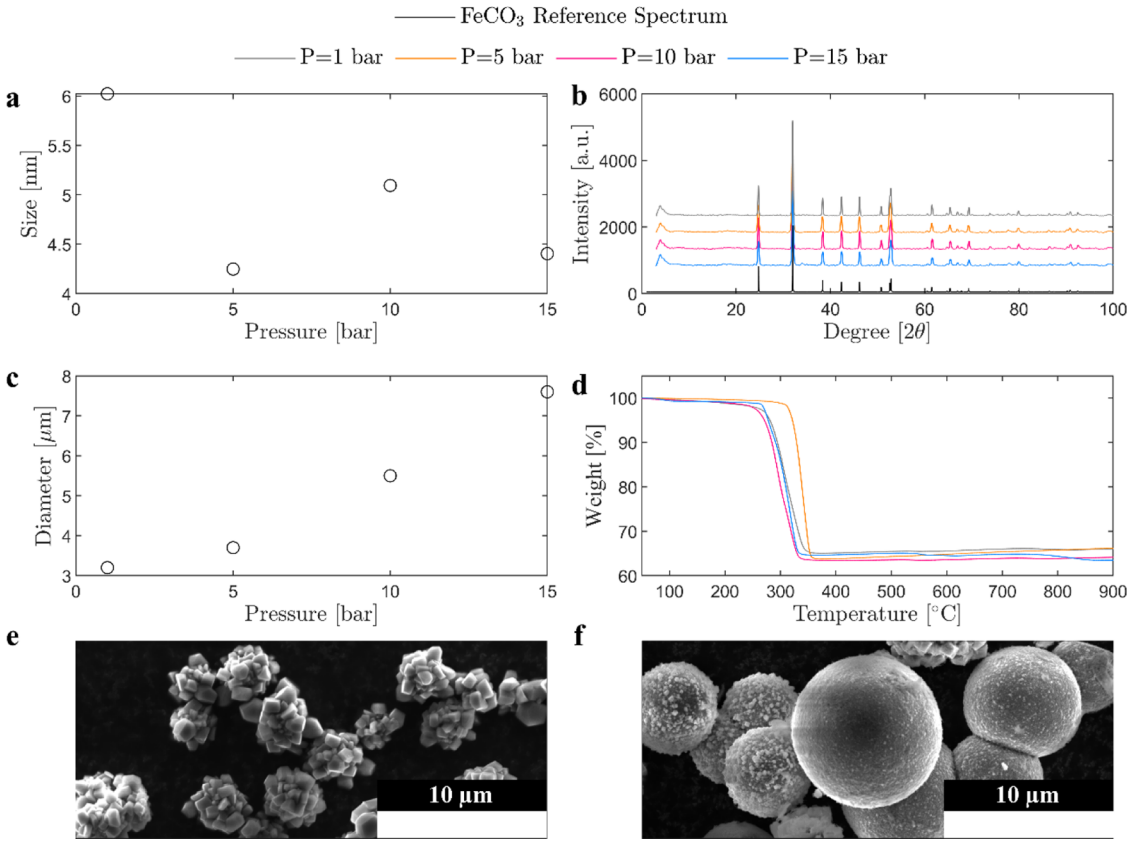

Figure 7. (a) Particle size (nm) as a function of pressure, (b) XRPD spectra of $FeCO_3$ synthesized at varying pressures for 24 h at 130 °C, (c) particle diameter (μm) as a function of pressure, and (d) TGA curves of $FeCO_3$. SEM image of the synthesis product performed at (e) 1 and (f) 15 bar.

sizes.[76] Kim et al.[76] observed that at least after one week the reaction was fully converted to $FeCO_3$ with particle sizes of 10 μm. While the particle diameter increases linearly with temperature, the temperature has a more discrete effect on the crystallite sizes, as can be observed in Figure 5a. We refer to the diameter of the particles observable by SEM as the particle diameter and the size of the crystallite domains through the size, see Figure 5d for an illustrative example. The size of crystallite increased until an upper limit for the mean particle size of 5.8 μm was observed. Above 80 °C, the temperature's influence on the particle diameter seemed to be non-existing.

3.3.3. Thermal Decomposition Analysis. The thermal decomposition of $FeCO_3$ was measured using TGA. The results are presented in Figure 5d as a function of weight loss (%) versus temperature (°C). The thermal degradation is to a large degree influenced by the synthesis temperature. A weight loss of 36% initiating at 340 °C was found for the synthesis product made at 130 °C, while a total weight loss of 32% was found for the synthesis products made at 25 and 80 °C. Furthermore, the degradation was initiated at a lower temperature, with a slope of the weight loss being more moderate. There is a clear difference in the slopes at higher temperatures, while the synthesis performed at 130 °C gives a constant mass value, there is an additional weight loss from the primary degradation point up until the end temperature investigated (Figure 5d). As discussed, the synthesis is likely not fully converted to $FeCO_3$, and therefore the product synthesized at 25 and 80 °C has one additional degradation step. The additional degradation steps must be associated with unreacted $FeCl_2$ and Na_2CO_3, which were identified in the XRPD spectra, Figure 5b. The thermal degradation of $FeCO_3$ is important, as $FeCO_3$ could be incorporated in novel CO_2 capture processes. By having Fe_3O_4 reacting with CO_2, it could form $FeCO_3$, which when exposed to high temperatures would react back to the ferrous oxide. This mechanism was proposed in the work by Mendoza et al.[11]

3.4. Synthesis Duration. *3.4.1. Microscopic Analysis.* The XRPD spectra of $FeCO_3$ synthesized at different reaction durations are shown in Figure 6b, including the reference spectrum (black). The product synthesized for 4 h is the top spectrum, and $FeCO_3$ synthesized for 96 h is the second from the bottom in Figure 6b. Phases attributed to $FeCO_3$ were identified for XRPD spectra for $FeCO_3$ synthesized at 24 h or longer, Figure 6b. For spectra with a synthesis duration shorter than 24 h an extra peak was found at 34°, which was attributed to Na_2CO_3. Similar to the temperature, there is a cut of value for which the synthesis is not fully converted. For synthesis performed 4−12 h, the residue non-reacted Na_2CO_3 is observed in the spectra, Figure 6b. Longer reaction time has allowed for fully converted Na_2CO_3. There is a large spread in the duration of synthesis performed in the literature (see Table 1). Many researchers perform synthesis for much longer than 24 h.[27,31,32,39,43,54−56,60,61,63,68] These experiments are typically performed under high pressure and high temperature. There also exist a body of literature,[47,50,51] which have performed experiments at lower durations, however, they have reported a slight greenish color, which is indicative of unreacted $FeCl_2$.[47] Finally, claims are made stating that the reactants should react for a "sufficient" duration.[62] Discerning what a sufficient

https://doi.org/10.1021/acsomega.2c07303
ACS Omega 2023, 8, 3404−3414

duration is challenging without a thorough review of the obtained synthesis parameters, and therefore, we report that the reaction if fully converted after 24 h, however, the synthesis can be performed for longer durations if specific material properties are desired. Here we showcase how crystallite size and particle diameter can be tuned by changing the synthesis duration.

3.4.2. Particle Properties. Analyzing the SEM images, it was found that the reaction time increases the particle and the diameter size. In Figure 6a,c it is shown that there is an increase in grain size with the synthesis duration, which occurs in the same fashion as for the crystallite size. When the synthesis was performed shorter than 12 h, the size was found to be 3.8−4.7 μm, while when the synthesis performed was longer than 12 h, all particles had a larger mean diameter than 5.9 μm.

The size analysis (Figure 6a) showed that the crystallite size was in the range of 3.5−4.5 nm for less than 12 h, while synthesis performed for over 12 h had a crystallite size larger than 5 nm. The crystallite sizes seem to increase rapidly with a linear trend up to a synthesis reaction time of 24 h. Hereafter, the growth kinetics are gradually slowing down and the increase in the crystallite size is not as pronounced.

3.4.3. Thermal Analysis. The decomposition of $FeCO_3$ synthesized with varying reaction times is presented in Figure 6d. A slight decrease in weight loss occurs at 100 °C for $FeCO_3$ synthesized for 4 to 12 h. The same tendency, which was observed for $FeCO_3$ synthesized at 25, and 80 °C (Figure 5d), is seen for the shorter synthesis duration, 4 to 12 h. We hypothesize that the weight loss is caused by the evaporation of water, which is still present in the crystals after formation. Synthesis performed for 24 h or longer does not exhibit evaporation of water, and thereby indicates that an optimal synthesis duration exists where the product is fully formed. For the synthesis performed at 6 and 12 h, the mass loss slopes get gradually less smooth, and 32% of the weight is lost around 350 C, while for the synthesis performed for a longer time, there 36% of the mass is lost. Lastly, as the reaction time increases, the rate of mass loss increases, which indicates that a more uniform product is synthesized.

3.5. Impact of Pressure during Crystallization. *3.5.1. Microscopic Properties.* The phase composition and purity of the $FeCO_3$ synthesized for 24 h at 1, 5, 10, and 15 bar were confirmed by XRPD analysis (Figure 7b). The only crystalline phase was $FeCO_3$, as the obtained spectra of the product synthesized at 1−10 bar had the same diffraction peaks as the reference spectrum of $FeCO_3$. A single peak located at 34° was observed for the spectra of $FeCO_3$ synthesized at 15 bar and may be attributed to unreacted Na_2CO_3. The crystallite sizes as a function of increasing pressure are depicted in Figure 7. There is a large scatter in the data; however, a decreasing linear trend with increasing pressure might be present. The outlier at 5 bar is deviating from the observed trend. The outlier at 5 bar was also observed to have a brighter color from the color inspection (see Figure 7b). The origin of the this outlier could not be identified, but interestingly, the texture and color of the product synthesized under 5 bar are more similar to the synthesis performed for shorter than 12 h (light brown, aggregated, Figure 1a,b), than to the one synthesized at 1 and 10 bar. The crystallite size calculated for the product synthesized at 5 bar was similar to those synthesized for shorter durations than 12 h.

3.5.2. Particle Analysis. The particle size showed a pressure dependency (Figure 7), an increase in pressure increased the particle size. The largest particles were found for $FeCO_3$ synthesized at 15 bar. The particle size increased significantly by increasing the synthesis pressure. In addition to the diameter of particles being sensitive to the pressure under which they were synthesized, so was the particle morphology. No quantitative image characterization in terms of morphology; however, from visual inspection, a difference in morphology can be observed between the synthesis product yielded at 1 and 15 bar (Figure 7e,f). At 1 bar, they are clearly composed of rhombohedral structures growing from a common nucleation seed. While at 15 bar, the formed structures vary more in shape. The particles have a spherical structure, with smaller rhombohedral structures growing on the surface. Pressure has the largest effect on the macroscopic properties (particle diameter and particle morphology) out of the tested variables.

3.5.3. Thermal Analysis. The thermal degradation of $FeCO_3$ is presented in Figure 7d. No apparent trend is observed for $FeCO_3$ synthesized at varying pressures. The degradation is initiated earlier, approximately at 300 °C, for the $FeCO_3$ synthesized at 1, 5, and 15 bar compared to the one synthesized at 10 bar, which is initiated around 320 °C. There is also a small variation in the amount of degradation, which varies from a loss of 35−36.5%.

$FeCO_3$ synthesized at 1 bar has, besides the weight loss between 300 and 360 °C, two additional small decomposition peaks at 550 °C and at 830 °C, similar to those of $FeCO_3$ synthesized with the reaction times of 4−12 h (Figure 6d). The additional degradation slopes indicate that the produced $FeCO_3$ is not pure. The XRPD spectra also revealed additional peaks which were attributed to unreacted $FeCl_2{\cdot}4H_2O$ and Na_2CO_3. The reason for the extra degradation steps is, most likely, due to the degradation of $FeCl_2{\cdot}4H_2O$ and Na_2CO_3.

3.6. Effect of Size on Thermal Properties. In most of the TGA experiments, a decrease in weight loss is seen around 100 °C. This is due to the evaporation of water. Two degradation paths could be observed from the TGA experiments. One with a flat profile and a sharp onset at 340 °C, where approximately 36% of the weight was lost. No more changes occur up to a temperature of 900 °C. The weight loss of ∼36% would be consistent with a decarbonation according to the following reaction

$$4FeCO_3(s) \rightarrow Fe_3O_4(s) + Fe(s) + 4CO_2(g) \quad (2)$$

as the weight loss (decrease) associated with the release of CO_2 would be 38%.

The other path had an inclined curve, where the degradation was not defined for a sharp onset, but several weight losses were observed at 340, 600, and 800 °C. At 340 °C, approximately 32% of the weight was lost. This can be explained by the reaction presented below

$$6FeCO_3(s) \rightarrow 2Fe_3O_4(s) + C(s) + 5CO_2(g) \quad (3)$$

for which the release of CO_2 due to decarbonation would result in a weight loss of 31.7%.

The first path of degradation is what would be associated with pure $FeCO_3$. This was found for reactions synthesized longer than 12 h, temperature higher than 80 °C, and for all of the synthesis where the pressure was varied. These specific syntheses yielded products with a scattering coherence length larger than 3.3 Å. By relating these syntheses to their respective

https://doi.org/10.1021/acsomega.2c07303
ACS Omega 2023, 8, 3404−3414

TGA, it becomes apparent that synthesis products with crystallite sizes larger than 3.3 Å result in a degradation pathway of the second kind. The particle size obtained from SEM analysis cannot be linked to the thermal degradation. Therefore, it can be concluded that the thermal properties are mostly dependent on the properties of the crystallites.

4. CONCLUSIONS

The study of $FeCO_3$ is important in the prediction of CO_2 corrosion and mineralization processes. Detailed knowledge of the physical−chemical properties creates a better understanding of $FeCO_3$ and will lead to better prediction of corrosion and prevent costly shut downs in the maintenance process. The synthesis of $FeCO_3$ has been studied in this work with varying synthesis parameters such as temperature, reaction time, and pressure. Results showed that at synthesis reaction times less than 24 h and temperatures below 80 °C $FeCO_3$ synthesis was not complete, and peaks attributed to unreacted $FeCl_2$ and Na_2CO_3 were observed in the XRPD spectra. Particle sizes, in general, increased on varying synthesis parameters. TGA results showed two degradation paths with 32 and 36% weight losses. The path with 36% weight loss was found in products synthesized with reaction times longer than 12 h and temperatures higher than 80 °C, and in all of the syntheses where the pressure was varied.

AUTHOR INFORMATION

Corresponding Author

Philip L. Fosbøl − *Center for Energy Resources Engineering (CERE), Department of Chemical and Biochemical Engineering, Technical University of Denmark (DTU), 2800 Kongens Lyngby, Denmark;* orcid.org/0000-0003-1067-2348; Phone: +45 4525 2868; Email: plf@kt.dtu.dk

Authors

Randi Neerup − *Center for Energy Resources Engineering (CERE), Department of Chemical and Biochemical Engineering, Technical University of Denmark (DTU), 2800 Kongens Lyngby, Denmark;* orcid.org/0000-0003-1322-4436

Isaac A. Løge − *Center for Energy Resources Engineering (CERE), Department of Chemical and Biochemical Engineering, Technical University of Denmark (DTU), 2800 Kongens Lyngby, Denmark*

Complete contact information is available at: https://pubs.acs.org/10.1021/acsomega.2c07303

Author Contributions

The manuscript was written through contributions of all authors. All authors have given their approval to the final version of the manuscript.

Notes

The authors declare no competing financial interest.

ACKNOWLEDGMENTS

We acknowledge funding from the DTU Offshore through the project CO_2 impact on corrosion product ($FeCO_3$) solubility (CTR.2 D.15, LR_21) and financial support from the DTU Chemical Engineering Center for Energy Resources Engineering (CERE).

ABBREVIATIONS

AFC, amorphous $FeCO_3$; DO, dissolved oxygen; SEM, scanning electron microscopy; TEM, transmission electron microscopy; TGA, thermogravimetric analysis; XRPD, X-ray powder diffraction

REFERENCES

(1) Kumar, S.; Drozd, V.; Durygin, A.; Saxena, S. K. Capturing CO2 Emissions in the Iron Industries using a Magnetite-Iron Mixture. *Energy Technol.* **2016**, *4*, 560−564.

(2) Kelektsoglou, K. Carbon capture and storage: A review of mineral storage of CO2 in Greece. *Sustain* **2018**, *10*, 4400.

(3) Islam, M. M.; Pojtanabuntoeng, T.; Gubner, R. Condensation corrosion of carbon steel at low to moderate surface temperature and iron carbonate precipitation kinetics. *Corros. Sci.* **2016**, *111*, 139−150.

(4) Ren, C.; Wang, W.; Jin, X.; Liu, L.; Shi, T. Physicochemical performance of FeCO3 films influenced by anions. *RSC Adv.* **2015**, *5*, 20302−20308.

(5) Fosbøl, P. L.; Thomsen, K.; Stenby, E. H. Review and recommended thermodynamic properties of FeCO3. *Corros. Eng., Sci. Technol.* **2010**, *45*, 115−135.

(6) Yen, C. P.; Wong, C. S.; Yeh, C. Y.; Chen, Y. M.; Chu, H. H.; Lin, J. Y.; Wang, J.; Lin, P. H.; Chen, S. Y. Growth of strongly textured FeCO3 thin films for application in research of nuclear quantum optics with ultrashort-pulsed laser deposition. *Appl. Phys. A: Mater. Sci. Process.* **2014**, *115*, 671−677.

(7) Benavente, R.; Lopez-Tejedor, D.; Palomo, J. M. Synthesis of a superparamagnetic ultrathin FeCO3 nanorods-enzyme bionanohybrid as a novel heterogeneous catalyst. *Chem. Commun.* **2018**, *54*, 6256−6259.

(8) Huang, Y.; Li, Y.; Huang, R.; Yao, J. Ternary Fe2O3/Fe3O4/FeCO3 Composite as a High-Performance Anode Material for Lithium-Ion Batteries. *J. Phys. Chem. C* **2019**, *123*, 12614−12622.

(9) Zhang, C.; Liu, W.; Chen, D.; Huang, J.; Yu, X.; Huang, X.; Fang, Y. One Step Hydrothermal Synthesis of FeCO3 Cubes for High Performance Lithium-ion Battery Anodes. *Electrochim. Acta* **2015**, *182*, 559−564.

(10) Liu, X.; Yang, S.; Chen, X.; Zheng, H.; Guo, Z.; Feng, C. Synthesis and electrochemical properties of FeCO3 with different morphology for lithium-ion battery application. *J. Alloys Compd.* **2017**, *698*, 87−93.

(11) Mendoza, M. E. Y.; Santos, A. S.; López, E. V.; Drozd, V.; Durygin, A.; Chen, J.; Saxena, S. K. Iron oxides as efficient sorbents for CO2 capture. *J. Mater. Res. Technol.* **2019**, *8*, 2944−2956.

(12) Weis, C.; Sternemann, C.; Cerantola, V.; Sahle, C. J.; Spiekermann, G.; Harder, M.; Forov, Y.; Kononov, A.; Sakrowski, R.; Yavaş, H.; Tolan, M.; Wilke, M. Pressure driven spin transition in siderite and magnesiosiderite single crystals. *Sci. Rep.* **2017**, *7*, 16526.

(13) Ponomar, V. P.; Dudchenko, N. O.; Brik, A. B. Phase transformations of siderite ore by the thermomagnetic analysis data. *J. Magn. Magn. Mater.* **2017**, *423*, 373−378.

(14) Golosova, N. O.; Kozlenko, D. P.; Dubrovinsky, L. S.; Cerantola, V.; Bykov, M.; Bykova, E.; Kichanov, S. E.; Lukin, E. V.; Savenko, B. N.; Ponomareva, A. V.; Abrikosov, I. A. Magnetic and structural properties of FeCO3 at high pressures. *Phys. Rev. B* **2017**, *96*, 134405.

(15) Stekiel, M.; Nguyen-Thanh, T.; Chariton, S.; McCammon, S.; Bosak, C.; Morgenroth, A.; Milman, W.; Refson, V.; Winkler, K.; Winkler, B. High pressure elasticity of FeCO3-MgCO3 carbonates. *Phys. Earth Planet. Inter.* **2017**, *271*, 57−63.

(16) Cerantola, V.; Bykova, E.; Kupenko, I.; Merlini, M.; Ismailova, L.; McCammon, C.; Bykov, M.; Chumakov, A. I.; Petitgirard, S.; Kantor, I.; Svitlyk, V.; Jacobs, J.; Hanfland, M.; Mezouar, M.; Prescher, C.; Rüffer, R.; Prakapenka, V. B.; Dubrovinsky, L. Stability of iron-bearing carbonates in the deep Earth's interior. *Nat. Commun.* **2017**, *8*, 15960.

(17) Santoso, R. K.; Rahmawati, S. D.; Gadesa, A.; Wahyuningrum, D. Understanding Passive Layer Formation for Further Corrosion

https://doi.org/10.1021/acsomega.2c07303
ACS Omega 2023, 8, 3404−3414

Management in Gas Production Pipes. *J. Phys.: Conf. Ser.* **2017**, *877*, 012062.
(18) Santoso, R. K.; Rahmawati, S. D.; Gadesa, A.; Wahyuningrum, D. Scale Build-Up Prediction of FeS and FeCO3 in Gas Production Pipes. *J. Phys.: Conf. Ser.* **2017**, *877*, 12029.
(19) Blondes, M. S.; Merrill, M. D.; Anderson, S. T.; DeVera, C. A. Carbon dioxide mineralization feasibility in the United States. *U.S. Geological Survey Scientific Investigations Report 2018−5079*, 2019.
(20) Matter, J. M.; Broecker, W. S.; Stute, M.; Gislason, H.; Oelkers, A.; Stefánsson, H. A.; Wolff-Boenisch, E. S.; Gunnlaugsson, G.; Axelsson, B.; Björnsson, D. Permanent Carbon Dioxide Storage into Basalt: The CarbFix Pilot Project, Iceland. *Energy Procedia* **2009**, *1*, 3641−3646.
(21) Matter, J. M.; Broecker, W. S.; Gislason, S. R.; Gunnlaugsson, E. H.; Oelkers, A.; Stute, D.; Sigurdardóttir, E.; Stefansson, G.; Alfreosson, G.; Aradóttir, E. S.; Axelsson, G.; Sigfússon, B.; Wolff-Boenisch, D. The CarbFix Pilot Project - Storing carbon dioxide in basalt. *Energy Procedia* **2011**, *4*, 5579−5585.
(22) Mendoza, E. Y. M.; Santos, A. S.; López, E. V.; Durygin, A.; Chen, J.; Saxena, S. K. Siderite formation by mechanochemical and high pressure-high temperature processes for CO2 capture using iron ore as the initial sorbent. *Processes* **2019**, *7*, 735.
(23) Barker, R.; Burkle, D.; Charpentier, T.; Thompson, H.; Neville, A. A review of iron carbonate (FeCO3) formation in the oil and gas industry. *Corros. Sci.* **2018**, *142*, 312−341.
(24) Burkle, D. P. Understanding the Formation of Protective FeCO3 on to Carbon Steel Pipelines during CO2 Corrosion. Ph.D. Thesis, The University of Leeds, 2017.
(25) Mcguire, S. O.; Miller, W. J.; Gentry, R. P.; Neathery, M. W.; Ho, S. Y.; Blackmon, D. M. Influence of High Dietary Iron as Ferrous Carbonate and Ferrous Sulfate on Iron Metabolism in Young Calves. *J. Dairy Sci.* **1985**, *68*, 2621−2628.
(26) Schwab, A. P.; Lindsay, W. L. Effect of Redox on the Solubility and Availability of Iron. *Soil Sci. Soc. Am. J.* **1983**, *47*, 201−205.
(27) Singer, P. C.; Stumm, W. The Solubility of ferrous iron in carbonate-bearing waters. *J.—Am. Water Works Assoc.* **1970**, *62*, 198−202.
(28) Ha, J.; Zhao, X.; Yu, R.; Barkay, T.; Yee, N. Hg(II) reduction by siderite (FeCO3). *Appl. Geochem.* **2017**, *78*, 211−218.
(29) Bibi, I.; Niazi, N. K.; Choppala, G.; Burton, E. D. Chromium(VI) removal by siderite (FeCO3) in anoxic aqueous solutions: An X-ray absorption spectroscopy investigation. *Sci. Total Environ.* **2018**, *640−641*, 1424−1431.
(30) Smith, H. J. On equilibrium in the system: ferrous carbonate, carbon dioxide and water. *J. Am. Chem. Soc.* **1918**, *40*, 879−883.
(31) Sharp, W. E. The cell constants of artificial siderite. *Am. Mineral.* **1960**, *45*, 241−243.
(32) Kiss, M. L.; Chirita, M.; Ercuta, A.; Savii, C.; Ieta, A. Highly ordered nanostructured magnetite and maghemite of micrometric sized and rhombohedral habit. *Technical Proceedings of the 2014 NSTI Nanotechnology Conference and Expo*, NSTI-Nanotech 2014, 2014; Vol. *1*, pp 474−477.
(33) Gogolev, A. V.; Zakharova, E. V.; Rodygina, N. I.; Fedoseev, A. M.; Shilov, V. P. Reduction of neptunium(V) and uranium(VI) with iron(II) in bicarbonate solutions. *Radiochemistry* **2006**, *48*, 249−253.
(34) Yang, T.; Huang, Z.; Liu, Y.; Fang, M.; Ouyang, X.; Hu, M. Controlled Synthesis of Porous FeCO3 Microspheres and the Conversion to α-Fe2O3 with Unconventional Morphology. *Ceram. Int.* **2014**, *40*, 11975−11983.
(35) Sánchez-Alcalá, I.; Bellón, F.; del Campillo, M. C.; Barrón, V.; Torrent, J. Application of synthetic siderite (FeCO3) to the soil is capable of alleviating iron chlorosis in olive trees. *Sci. Hortic.* **2012**, *138*, 17−23.
(36) Zhang, S.; Lu, Y. Kinetic performance of CO2 absorption into a potassium carbonate solution promoted with the enzyme carbonic anhydrase: Comparison with a monoethanolamine solution. *Chem. Eng. J.* **2015**, *279*, 335−343.
(37) Graf, D. L. Crystallographic tables for the rhombohedral carbonates. *Am. Mineral.* **1961**, *46*, 1283−1316.
(38) Ehrhardt, H. v.; Schober, H. C.; Seidel, H. Hochdrucksynthesen von Carbonaten. III. Darstellung von Carbonaten zweiwertiger Metalle durch Zersetzung ihrer Oxalate unter hohem CO2-Druck. *Z. Anorg. Allg. Chem.* **1980**, *465*, 83−91.
(39) Greenberg, J.; Tomson, M. Precipitation and dissolution kinetics and equilibria of aqueous ferrous carbonate vs temperature. *Appl. Geochem.* **1992**, *7*, 185−190.
(40) Wersin, P.; Charlet, L.; Karthein, R.; Stumm, W. From adsorption to precipitation: Sorption of Mn2+ on FeCO3(s). *Geochim. Cosmochim. Acta* **1989**, *53*, 2787−2796.
(41) Bruno, J.; Wersin, P.; Stumm, W. On the influence of carbonate in mineral dissolution: II. The solubility of FeCO3 (s) at 25°C and 1 atm total pressure. *Geochim. Cosmochim. Acta* **1992**, *56*, 1149−1155.
(42) Heuer, J. K.; Stubbins, J. F. An XPS characterization of FeCO3 films from CO2 corrosion. *Corros. Sci.* **1999**, *41*, 1231−1243.
(43) Chirita, M.; Banica, R.; Ieta, A.; Bucur, A.; Sfiarloaga, P.; Ursu, D. H.; Grozescu, I. Highly Crystalline Microparticle Synthesis by Hydrothermal Decomposition of Fe- EDTA Complex. *AIP Conf. Proc.* **2010**, *1262*, 124−129.
(44) Chirita, M.; Banica, R.; Sfirloaga, P.; Ieta, A.; Grozescu, I. A short route of micrometric magnetite synthesis via Fe-EDTA thermal decomposition. *Proc. Int. Semicond. Conf. CAS* **2010**, *2*, 391−394.
(45) Liu, X.; Wang, H.; Su, C.; Zhang, P.; Bai, J. Controlled fabrication and characterization of microspherical FeCO3 and α-Fe2O3. *J. Colloid Interface Sci.* **2010**, *351*, 427−432.
(46) Zhong, Y.; Su, L.; Yang, M.; Wei, J.; Zhou, Z. Rambutan-like FeCO3 hollow microspheres: Facile preparation and superior lithium storage performances. *ACS Appl. Mater. Interfaces* **2013**, *5*, 11212−11217.
(47) Figueiredo, C. M. S.; Junior, A. G., Jr.; Flaten, E. M.; Beck, R.; Seiersten, M. Crystal growth of FeCO3 in mixed monoethylene glycol and water solvent. *Cryst. Res. Technol.* **2015**, *50*, 354−361.
(48) Feng, X.; Shen, Q.; Shi, Y.; Zhang, J. Morphology-controlled hydrothermal synthesis of acanthosphere FeCO3 as an excellent performance anode material for lithium ion batteries. *Ceram. Int.* **2016**, *42*, 14246−14251.
(49) Liang, W.; Yin, Y.; Li, Z.; Li, R.; Li, L.; He, Y.; Dong, H.; Li, Z.; Yan, S.; Zhai, S.; Li, H. Single crystal growth, crystalline structure investigation and high-pressure behavior of impurity-free siderite (FeCO3). *Phys. Chem. Miner.* **2018**, *45*, 831−842.
(50) Wajon, J. E.; Ho, G. E.; Murphy, P. J. Rate of precipitation of ferrous iron and formation of mixed iron-calcium carbonates by naturally occurring carbonate materials. *Water Res.* **1985**, *19*, 831−837.
(51) Murcia, D. C. F. High Pressure High Temperature Reservoir Fluids with Focus on Scaling and Thermodynamic Modeling. P.h.D Thesis, Technical University of Denmark, 2018.
(52) Tomson, M. B.; Johnson, M. L. How Ferrous Carbonate Kinetics Impacts Oilfield Corrosion. *SPE International Symposium on Oilfield Chemistry*, 1991; SPE-21025-MS.
(53) Ptacek, C. J. Experimental determination of siderite solubility in high ionic-strength aqueous solutions. Ph.D. Thesis, University of Waterloo, 1992.
(54) Kang, N.; Schmidt, M. W.; Poli, S.; Franzolin, E.; Connolly, J. A. D. Melting of siderite to 20GPa and thermodynamic properties of FeCO3-melt. *Chem. Geol.* **2015**, *400*, 34−43.
(55) Chai, L.; Navrotsky, A. Enthalpy of formation of siderite and its application in phase equilibrium calculation. *Am. Mineral.* **1994**, *79*, 921−929.
(56) Ehrhardt, H.; Seidel, H.; Schweer, H. Hochdrucksynthesen einiger Carbonate mit überkritischem CO2. *Z. Anorg. Allg. Chem.* **1980**, *462*, 185−198.
(57) Johnson, M. L. Ferrous carbonate precipitation kinetics: A temperature ramped approach. Ph.D. Thesis, Rice University, 1991.
(58) Johannes, W. Experimentelle Sideritbildung aus Calcit + FeCl2. *Contrib. Mineral. Petrol.* **1968**, *17*, 155−164.
(59) Gould, F. T. Process for preparing chemically pure ferrous carbonate. U.S. Patent 3,416,883 A, 1968.

https://doi.org/10.1021/acsomega.2c07303
ACS Omega 2023, 8, 3404−3414

(60) Gamsjäger, H.; Reiterer, F. Investigation of Equilibria Involving Carbon Dioxide, Carbonates and Water. *Environ. Int.* **1979**, *2*, 419−424.
(61) Stubina, N. M.; Toguri, J. M. Decomposition pressure of synthetic siderite (FeCO3). *Iron and Steelmaker* **1988**, *15*, 63−66.
(62) Lyon, W. G. Process for Preparing Ferrous Carbonate. U.S.Patent 4,657,752 A, 1987.
(63) Silva, C. A. R.; Liu, X.; Millero, F. J. Solubility of Siderite (FeCO3) in NaCl Solutions. *J. Solution Chem.* **2002**, *31*, 97−108.
(64) Jimenez-Lopez, C.; Romanek, C. S. Precipitation kinetics and carbon isotope partitioning of inorganic siderite at 25°C and 1 atm. *Geochim. Cosmochim. Acta* **2004**, *68*, 557−571.
(65) Romanek, C. S.; Jiménez-López, C.; Navarro, A. R.; Sánchez-Román, M.; Sahai, N.; Coleman, M. Inorganic synthesis of Fe-Ca-Mg carbonates at low temperature. *Geochim. Cosmochim. Acta* **2009**, *73*, 5361−5376.
(66) Koo, T.-h.; Kim, J. Controls on the formation and stability of siderite (FeCO3) and chukanovite (Fe2(CO3)(OH)2) in reducing environment. *Minerals* **2020**, *10*, 156.
(67) Sel, O.; Radha, A. V.; Dideriksen, K.; Navrotsky, A. Amorphous iron (II) carbonate: Crystallization energetics and comparison to other carbonate minerals related to CO2 sequestration. *Geochim. Cosmochim. Acta* **2012**, *87*, 61−68.
(68) Chirita, M.; Ieta, A. FeCO3 microparticle synthesis by Fe-EDTA hydrothermal decomposition. *Cryst. Growth Des.* **2012**, *12*, 883−886.
(69) Rahman, I. A.; Vejayakumaran, P.; Sipaut, C. S.; Ismail, J.; Bakar, M.; Adnan, R.; Chee, C. K. An optimized sol-gel synthesis of stable primary equivalent silica particles. *Colloids Surf., A* **2007**, *294*, 102−110.
(70) Wang, H. C.; Wu, C. Y.; Chung, C. C.; Lai, M. H.; Chung, T. W. Analysis of parameters and interaction between parameters in preparation of uniform silicon dioxide nanoparticles using response surface methodology. *Ind. Eng. Chem. Res.* **2006**, *45*, 8043−8048.
(71) Kim, K. D.; Kim, H. T. Formation of silica nanoparticles by hydrolysis of TEOS using a mixed semi-batch/batch method. *J. Sol-Gel Sci. Technol.* **2002**, *25*, 183−189.
(72) Tan, C. G.; Bowen, B. D.; Epstein, N. Production of monodisperse colloidal silica spheres: Effect of temperature. *J. Colloid Interface Sci.* **1987**, *118*, 290−293.
(73) Meier, M.; Ungerer, J.; Klinge, M.; Nirschl, H. Synthesis of nanometric silica particles via a modified Stöber synthesis route. *Colloids Surf., A* **2018**, *538*, 559−564.
(74) Pierre, A. C. *Introduction to Sol-Gel Processing. The International Series in Sol-Gel Processing: Technology & Applications*; Springer, 1998; p 394.
(75) Satoh, T.; Akitaya, M.; Konno, M.; Saito, S. Particle size distributions produced by hydrolysis and condensation of tetraethylorthosilicate. *J. Chem. Eng. Jpn.* **1997**, *30*, 759−762.
(76) Kim, S.; Marrs, C.; Nemer, M.; Je-Hun Jang, J. J. Solubility Model for Ferrous Iron Hydroxide, Hibbingite, Siderite, and Chukanovite in High Saline Solutions of Sodium Chloride, Sodium Sulfate, and Sodium Carbonate. *ACS Earth Space Chem.* **2017**, *1*, 647−663.

https://doi.org/10.1021/acsomega.2c07303
ACS Omega 2023, 8, 3404−3414